Multi-phase Transformation of NaFeF$_3$ During Desodiation and Sodiation

Yayun Zheng,[†] Shunta Jitto,[†] Jinkwang Hwang,[†,‡] Kazuhiko Matsumoto[,†,‡] and Rika Hagiwara[†,‡]*

†Graduate School of Energy Science, Kyoto University, Yoshida-honmachi, Sakyo-ku, Kyoto

606-8501, Japan

‡Unit of Elements Strategy Initiative for Catalysts & Batteries (ESICB), Kyoto University,

Katsura, Kyoto 615-8510, Japan.

ABSTRACT: The orthorhombic $NaFeF_3$, which is envisioned to be an auspicious positive electrode for Na-ion batteries, has drawn considerable interest as an environmentally benign energy material with exceptional high theoretical capacity. Despite these prospects, the reaction mechanism(s) during orthorhombic $NaFeF_3$ operations are still not well understood. Thus, in a bid to expound on this research space, we report the reaction mechanism(s) of a carbon-coated orthorhombic $NaFeF_3$ prepared through high-energy ball milling and heat treatment processes. A thermally stable ionic liquid electrolyte at elevated temperatures is employed to maximize the utilization of $NaFeF_3$. The orthorhombic $NaFeF_3$ exhibits high electrochemical activity and long-term cycling stability of up to 400 cycles at 90 °C. Through a combination of galvanostatic intermittent titration technique and synchrotron X-ray powder diffraction measurements, we discover that the (de)sodiation processes are facilitated by a multi-phase transformation mechanism. Further, we experimentally identify, for the first time, an orthorhombic $Na_{0.5}FeF_3$ compound as an intermediate phase of the transformations. The results discussed in this work are expected to provide invaluable insights for the future advancement of the Na-Fe-F system.

INTRODUCTION

Lithium-ion batteries (LIBs) have become the bedrock of modern technological innovations, embodying the yardstick for energy storage devices with high energy- and power densities. Despite this dominance, the viability of lithium-based chemistries for future energy applications is heavily saddled with concerns over the rapidly depleting lithium resources, invigorating explorations into sustainable chemistries such as sodium.[1-2] Over the years, sodium-ion batteries (SIBs) have extensively aroused interest as potential LIB replacements in large-scale energy storage applications due to the terrestrial and oceanic abundance of sodium (fourth most abundant element) and their low costs of production.[3-5] Furthermore, similarities in the physical and chemical properties of sodium and lithium (both group 1A elements) augur the possibilities of high SIBs performances that are comparable to LIBs.[2]

In the search for next-generation battery materials, iron fluorides have gained interest as functional positive electrodes for LIBs and SIBs due to the abundance of iron resources and the superior output voltages proffered by the highly electronegative fluorine.[6-9] An exemplar of these materials, iron trifluoride (FeF_3), has been found to deliver an exceptional theoretical capacity of 712 mAh g^{-1} (over three times higher than oxide- and polyanionic-based positive electrodes) *via* a three-electron transfer process that involves the conversion of FeF_3 into a mixture of zero-valent Fe and alkaline metal fluoride (LiF or NaF).[10-11] This outstanding electrochemical performance has prompted numerous inquests into the phase transitions facilitating the lithiation of trigonal

FeF$_3$ ($R\bar{3}c$) in the Li-Fe-F system.[12-16] Reports on this subject have revealed the initial lithium insertion to engender a phase transition from the trigonal FeF$_3$ ($R\bar{3}c$) to a trirutile Li$_{0.5}$FeF$_3$ ($P4_2/mnm$) structure with edge- and corner-sharing FeF$_6$ octahedra. Continued lithiation into the trirutile Li$_{0.5}$FeF$_3$ phase is reported to facilitate a conversion reaction involving complex displacement reaction mechanisms, which forms a mixture of LiF and FeF$_2$.[13-16] The conversion reaction from the LiF/FeF$_2$ mixture to FeF$_3$ during the delithiation is also confirmed.[17] Further, deep lithiation involves a reaction between FeF$_2$ and two Li$^+$ ions, triggering a conversion reaction from FeF$_2$ to zero-valent Fe and LiF.[15, 18-19]

Despite the great strides made to elucidate the phase evolution of FeF$_3$ in the Li-Fe-F system, the corresponding mechanisms in the Na-Fe-F system are still not well established.[10-11, 20-28] In attempts to unravel desodiation properties of orthorhombic NaFeF$_3$, density functional theory (DFT) calculations have shown the orthorhombic Na$_{0.5}$FeF$_3$ ($Pnma$) phase to be the only energetically stable intermediate phase formed during a one-electron reaction between an orthorhombic NaFeF$_3$ ($Pnma$) and a fully desodiated orthorhombic FeF$_3$ ($Pnma$).[29-30] Although the DFT calculation showed the orthorhombic FeF$_3$ ($Pnma$) is slightly more stable than the ones with the trigonal ($R\bar{3}c$) and cubic ($Pm\bar{3}m$) phases, the difference was very little - implying possible susceptibility to overturn the order under certain external factors. As has been reported by a previous experimental study, desodiation of orthorhombic NaFeF$_3$ nanoparticles forms a cubic FeF$_3$ ($Pm\bar{3}m$) framework of corner-sharing FeF$_6$ octahedra.[31] Other experimental works found a

FeF$_3$ starting material to undergo transformation into NaFeF$_3$ during the sodiation process but could not confirm the integrant phase structure(s) nor the existence of any intermediate Na$_x$FeF$_3$ phase.[25, 32] In order to expand the understanding of the phase transition in the Na-Fe-F system, our previous work employed tetragonal FeF$_3$ derived from trirutile Li$_{0.5}$FeF$_3$ as the starting material and clarified the formation of a disordered trirutile Na$_x$FeF$_3$ during the sodiation process.[33] Along with further cycling, the structural transition between the tetragonal FeF$_3$ and the cubic FeF$_3$ phases was identified at the charged state as a result of reversible phase transformation between cubic FeF$_3$ and orthorhombic NaFeF$_3$ phases. It should be noted that although scientific interest in the Na-Fe-F system has increased in recent years, concrete experimental evidence and discussions pertaining to an intermediate Na$_x$FeF$_3$ phase remain scanty to date. As such, the experimental validation of a stable Na$_{0.5}$FeF$_3$ phase as an intermediate product of the (de)sodiation processes is expected to be a lynchpin in the progress of Na-Fe-F systems.

On the one hand, the experimental verification of a stable Na$_{0.5}$FeF$_3$ intermediate phase put forward high requirements for the crystallinity of electrodes. However, our previous works have confirmed that highly crystalline fluoride electrodes often show extremely low electrochemical activity under conventional conditions. In such cases, elevated-temperature operation of 90 °C using thermally stable ionic liquids (ILs) without introducing special peripheral materials effectively ameliorated the performance of such high crystalline electrode materials.[19, 33-35]

Moreover, batteries of elevated-temperature operations create a new avenue for utilizing the ubiquitous waste heat in daily activities, especially in large scale applications.[36-40]

Considering the research findings mentioned above, employing orthorhombic $NaFeF_3$ as the starting material is postulated to be a prudent approach to gaining a better insight into the phase evolution in the Na-Fe-F system. Thus, in an attempt to exploit this approach, we report the electrochemical performance and phase evolution of moderately crystalline $NaFeF_3$ with an orthorhombic phase prepared using a series of high-energy ball milling and heat treatment techniques. The electrochemical properties of the $NaFeF_3$ electrode were assessed at elevated temperatures (90 °C) using half- and symmetric cells comprising a thermally and chemically stable IL electrolytes. The present electrolyte was selected on account of the excellent solid-electrolyte interphase (SEI) forming capabilities and wide operation temperature ranges previously reported among IL electrolytes in SIBs.[38-39, 41-47] In this study, we ascertain the formation of an orthorhombic $Na_{0.5}FeF_3$ intermediate phase through a combination of galvanostatic intermittent titration technique (GITT) measurements and X-ray diffraction (XRD) analyses which provide insight into the phase evolution occurring during the (de)sodiation processes. Given the excellent prospects presented by FeF_3-based electrodes, the electrochemical performance of the $NaFeF_3$ discussed here is expected to expound the Na-Fe-F system knowledgebase to develop a material-design platform for next-generation energy storage systems.

EXPERIMENTAL SECTION

All reagents used in the present work were stored and handled under a dry and deoxygenated Ar atmosphere (oxygen and water level < 1 ppm) in a glove box. Tetrahydrofuran (THF; dehydrated, Wako Pure Chemical Industries, water content < 10 ppm, stabilizer-free) and Na metal (Sigma-Aldrich, purity 99.95%) were used as purchased. NaF (Wako Pure Chemical Industries, purity 99%), FeF_2 (Sigma-Aldrich, purity 98%), acetylene black (AB; Wako Pure Chemical Industries, purity > 99.99%), and poly(tetrafluoroethylene) (PTFE; Sigma-Aldrich, Inc.; particle size: ca. 200 μm) were dried under vacuum at 120 °C before storage in the glove box. The FSA salts, Na[FSA] (FSA^-: bis(fluorosulfonyl)amide, Mitsubishi Materials Electronic Chemicals, purity > 99%) and $[C_2C_1im][FSA]$ ($C_2C_1im^+$: 1-ethyl-3-methylimidazolium, Kanto Chemical, purity > 99.9%) were dried under vacuum for 24 h at 80 °C. Battery-grade 1 mol dm^{-3} $NaPF_6$/EC:DMC (1:1 v/v, Kishida Chemical Co. Ltd.; EC: ethylene carbonate; DMC: dimethyl carbonate) organic electrolyte was used as purchased.

The present orthorhombic $NaFeF_3$ was prepared using a combination of ball milling and heat treatment procedures as illustrated in Figure 1. Equimolar amounts of NaF and FeF_2 were weighed and loaded into an airtight zirconia-lined bowl under the dry Ar atmosphere. Approximately 1 g of the mixture was then ball-milled using a planetary ball mill (Planetary Micro Mill PULVERISETTE 7 premium line, Fritsch) at 600 rpm for 6 h with the aid of zirconia balls (3 mm in diameter). After the ball milling process, the bowl was opened inside the glovebox, and the

collected sample (Pre-NaFeF$_3$) was transferred onto a nickel boat. The nickel boat was sealed inside a stainless-steel pipe in the glovebox and connected to a vacuum line via a valve. The Pre-NaFeF$_3$ was heated at 600 °C for 24 h under vacuum. After the heat treatment, the target sample of orthorhombic NaFeF$_3$ (H-NaFeF$_3$) was collected in the glovebox. The H-NaFeF$_3$ was then mixed with AB (75:25 in weight) and subjected to the ball milling process to form a carbon-coated sample (NaFeF$_3$@C) with enhanced electronic conductivity.

A homogeneous electrode sheet was prepared by thoroughly mixing PTFE binder with the NaFeF$_3$@C (NaFeF$_3$@C:PTFE = 95:5 in weight) sample using an agate mortar and a pestle. The sheet was thereafter pressed onto an Al mesh (13 mm in diameter) at a loading mass of ~ 3 mg cm^{-2} to prepare the test electrode. A separator was prepared by soaking a glass microfiber (Whatman, GF/A; 16 mm in diameter and 260 μm in thickness) in the Na[FSA]-[C$_2$C$_1$im][FSA] (20:80 in mol) ionic liquid (IL) electrolyte[43] under vacuum at 90 °C for 12 h. Coin cells (2032-type) comprising the NaFeF$_3$ working electrode, the IL-soaked separator, and a Na metal disk counter electrode pressed onto an Al plate current collector were assembled inside the Ar-filled glovebox.

The electrochemical data was obtained using an HJ-SD8 charge−discharge system (Hokuto Denko). The charge−discharge curves and cycling performance of the working electrode were evaluated through galvanostatic charge−discharge tests. In this study, the capacity of the positive electrode is presented as a value per weight (in grams) of NaFeF$_3$. The overpotentials of the

electrode were assessed *via* the galvanostatic intermittent titration technique (GITT), wherein the voltage relaxation of the cell was repeatedly monitored in the open-circuit state immediately after charging or discharging to a specific voltage. The electrochemical impedance spectra (EIS) measurements were performed using a VSP potentiostat (Bio-Logic) over a frequency range of 10 mHz–100 kHz with a perturbation amplitude of 10 mV. Symmetric cells (2032 coin-type) assembled using pre-charged electrodes (state of charge (SOC): 50%) obtained from half-cells with the IL electrolyte at 25 °C and 90 °C were subjected to EIS measurements at the corresponding temperatures. Additional EIS spectra were obtained from half-cells during cycling at the current rate of 100 mA g^{-1} at 90 °C. The half-cell measurements were taken at 3.2 V during the charging step of the *n*th cycle (*n* = 0, 1, 10, 20, 50, and 100).

The X-ray diffraction (XRD) patterns of $NaFeF_3$ at different synthetic stages were recorded in the Bragg−Brentano geometry, using a Rigaku MiniFlex diffractometer with Ni-filtered Cu-*Kα* radiation (30 kV and 10 mA) and a Si-strip high-speed detector (Rigaku D/tex Ultra250) at a scan rate of 1 deg min^{-1}. The morphology of the prepared $NaFeF_3$ powder was examined *via* field-emission scanning electron microscopy (SEM) (Hitachi SU-8020). The elemental distribution on the $NaFeF_3$ electrode surface was obtained through energy dispersion X-ray spectroscopic (EDX) mapping (Horiba EMAXEvolution). Detailed structural parameters of the $NaFeF_3$ electrodes at different SOCs were obtained through synchrotron XRD analysis performed at the BL5S2 of the Aichi Synchrotron Radiation Center equipped with a PILATUS 100 K two-dimensional detector

with a wavelength of 0.88603 Å. The electrode powders were washed with THF, vacuum-dried at

room temperature, and sealed in Lindeman glass capillaries. Rietveld refinement was used to

obtain the structural parameters by fitting the curves using the GSAS data analysis software.[48] The

VESTA program was used for crystal visualization.[49]

RESULTS AND DISCUSSION

The orthorhombic $NaFeF_3$ was prepared through a series of ball milling and heat treatment

techniques performed on NaF and FeF_2 precursor materials. The preparation process is

summarized in Figure 1. The XRD patterns shown in Figure S1 were obtained from samples taken

after the initial ball milling (Pre-$NaFeF_3$), initial heat treatment at 600 °C for 24h (H-$NaFeF_3$), and

subsequent ball milling with AB ($NaFeF_3$@C) to establish the structural evolution and purity of

the material at each preparation stage. The Pre-$NaFeF_3$ sample exhibited several broad peaks

assigned to NaF, FeF_2, and orthorhombic $NaFeF_3$ (Figure S1a), affirming that the complete

synthesis of orthorhombic $NaFeF_3$ could not be achieved through ball milling alone. After the

initial heat treatment at 600 °C for 24h (H-$NaFeF_3$ sample), the orthorhombic $NaFeF_3$ diffraction

peaks (Figure S1b) were observed to become sharper while those ascribed to FeF_2 and NaF

disappear—an indication that a pure orthorhombic $NaFeF_3$ phase had been formed. As shown in

Figure 2a, the XRD results were further analyzed using Rietveld refinement, which revealed that

the obtained H-$NaFeF_3$ lattice well-fitted within the parameters of a perovskite-related $NaFeF_3$ in

10

the *Pnma* space group (R_p = 1.33%, R_{wp} = 1.82%, a = 5.6577(2) Å, b = 7.8860(2) Å, and c = 5.4937(2) Å). The corresponding crystallographic parameters are furnished in Figure 2c and Table S1.

Subsequently, a carbon-coated sample (NaFeF$_3$@C) was prepared by ball milling a mixture of H-NaFeF$_3$ and AB to enhance the electronic conductivity of the material. The carbon-coated NaFeF$_3$@C displayed similar diffraction peaks as the H-NaFeF$_3$ (Figure S1c), although they appeared to be broader and weaker in intensity. Rietveld refinement of the XRD patterns (Figure 2b) confirmed that the orthorhombic structure had been preserved, with no significant differences noted between the NaFeF$_3$@C and H-NaFeF$_3$ lattice parameters (Figure 2c and Table S1). Therefore, it can be surmised that carbon-coating through ball milling did not deform the crystal structure of the present orthorhombic NaFeF$_3$ but only served to reduce the particle sizes. For clear visualization of the lattice structure, a schematic of the refined orthorhombic NaFeF$_3$ has been furnished in Figure 2d. As illustrated, each Na cation is coordinated to eight corner-sharing FeF$_6$ octahedron units. The corner-sharing FeF$_6$ octahedron units are found to render large spaces for Na$^+$ occupation, establishing diffusion paths along the [010] channels and the [101] and [−101] diagonals of the *ac*-plane.[31, 50-51]

For further characterization, SEM was employed to establish the particle size and morphology of the H-NaFeF$_3$ and NaFeF$_3$@C samples. The images in Figure 2e,f show that both samples have smooth-surfaced crystal particles. The H-NaFeF$_3$ particles are larger (between 200 nm to 1 μm)

than the NaFeF$_3$@C particles (~100 nm) due to the additional pulverization during the ball-milling process. The efficacy of the present synthesis process is further validated by EDX mapping, which revealed a homogeneous distribution of Na, Fe, F, and C within the NaFeF$_3$@C particles. However, it is worth noting that the orthorhombic NaFeF$_3$ diffraction peaks observed in the carbon-coated NaFeF$_3$@C were weaker than in the H-NaFeF$_3$. Thus, in an attempt to recover the diminished crystallinity, NaFeF$_3$@C was further heat-treated at 600 °C for 15 h under vacuum. The resulting sample (hereafter RH-NaFeF$_3$@C) displayed sharper orthorhombic NaFeF$_3$ diffraction peaks with no discernable phase transformation (Figure S2). The RH-NaFeF$_3$@C sample will be discussed in detail later in this section.

For insight into the electrochemical properties of the orthorhombic NaFeF$_3$, a Na/NaFeF$_3$@C half-cell configuration comprising a Na[FSA]-[C$_2$C$_1$im][FSA] (20:80 in mol) IL electrolyte was subjected to galvanostatic charge-discharge tests in the 2.2−4.1 V voltage range at a current rate of 10 mA g^{-1} (Figure 3). Considering the excellent thermostability proffered by the present electrolyte, the electrochemical performance of NaFeF$_3$@C was investigated at an elevated temperature of 90 °C, as shown in Figure 3a. During measurements at 90 °C, the electrode delivered a relatively high discharge capacity of 177 mAh g^{-1}—equivalent to a 0.9 Na$^+$ extraction/insertion (based on a theoretical capacity of 197 mAh g^{-1}) from/into the host lattice (Figure 3a-I). The charge-discharge curves from the first two cycles displayed two distinct pairs of plateaus appearing around 3.0 V and 3.4 V. The specific voltages of the plateaus were

established by the corresponding dQ/dV plots (Figure 3a-II), which depicted two pairs of redox peaks at 3.04/2.97 V and 3.36/3.12 V, respectively. This provides clear evidence for the multi-phase transformation of the orthorhombic NaFeF$_3$ during desodiation-sodiation processes. The plots additionally showed a peak emerging at 4.0 V during the initial charge process, revealing that electrolyte decomposition occurred at high voltages.[52-53]

The phase evolution(s) transpiring during the (de)sodiation processes at 90 °C were further investigated through GITT tests (Figure 3a-III). Here, the half-cell was subjected to a stepwise polarization at 10 mA g^{-1} for 1 h, whereafter the open-circuit voltage was monitored for 12 h. During the initial charge process, the potential after relaxation gradually increased before forming a plateau with a slight overvoltage at around 3.0 V. This observation suggests that the initial charge to this point involved a two-phase reaction. Further, the voltage was observed to continue rising, forming another plateau with a relatively constant open-circuit voltage at around 3.4 V. Afterwards, the open-circuit voltage above 3.4 V was visualized to increase with a gentle curve, suggesting the occurrence of a single-phase reaction in this region. Although the differences in voltage are somewhat indistinct during discharge, two plateaus around 3.2 V and 3.0 V were observed to appear with a larger solid-solution region at the lower voltage (< 3.0 V). This GITT result also proves the multi-phase transformation of the orthorhombic NaFeF$_3$ accompanied by Na$^+$ extraction/insertion reaction.

To gain perspective on the effects of temperature on the electrode behavior, the Na/NaFeF$_3$@C was subjected to galvanostatic charge-discharge measurements conducted at 25 °C under the previously prescribed conditions (Figure 3b). The first two cycles displayed two pairs of small plateaus in the 2.2−4.1 V voltage range, delivering a limited discharge capacity of 99.5 mAh g^{-1} (Figure 3b-I). The corresponding dQ/dV plots (Figure 3b-II) illustrated two pairs of broad redox peaks that depict the specific voltages of the plateaus. However, the redox peak representing the plateau at the higher voltage during discharge was indiscernible, attesting to the limited electrochemical activity at room temperature. Additionally, no clear plateaus were observed in the GITT profiles obtained during evaluation at 25 °C under the previously prescribed conditions, as shown in Figure 3b-III. The electrochemical performance of NaFeF$_3$@C at 25 °C was also measured in the NaPF$_6$-EC:DMC (1:1 v/v) organic electrolyte for comparison. As observed from the charge-discharge profiles (Figure S3a), NaFeF$_3$@C exhibits a discharge capacity of 104.3 mAh g^{-1} in the organic electrolyte which is similar to that the IL electrolyte at 25 °C. Severer oxidative decomposition of the electrolyte is observed in the organic electrolyte compared to the IL electrolyte. The corresponding dQ/dV plots in the organic electrolyte (Figure S3b) also exhibits two pairs of redox peaks, demonstrating NaFeF$_3$@C is involved with two two-phase transformations in the organic electrolyte at 25 °C. However, the capacity is still limited to evaluate phases during charge-discharge tests. The findings not only validate temperature elevation as an avenue for performance enhancement but also accentuate the practicality of ionic liquid electrolytes in such elevated temperature operations.

14

The underlying mechanisms behind the increased capacity during measurements at elevated temperatures (90 °C) were further investigated by performing EIS tests on NaFeF$_3$@C//Na[FSA]-[C$_2$C$_1$im][FSA]//NaFeF$_3$@C symmetric cells at 25 °C and 90 °C (Figure S4a,b). Prior to the symmetric cell assembly, the two constituent NaFeF$_3$@C electrodes were charged to a state of charge (SOC) of 50% in Na/NaFeF$_3$@C half cells at 25 °C and 90 °C, respectively. Nyquist plots comprising two semicircles that correspond to the cell resistance were fitted into the equivalent circuit shown in the inset of Figure S4b. When the temperature was increased from 25 °C to 90 °C, all resistances were noted to decrease (Table S2), attesting to ameliorated ion diffusion and consequently enhanced electrochemical activity of NaFeF$_3$@C at the elevated temperature.[47, 54-58] For a detailed perspective on the factors contributing to the resistance, the decrease noted in the bulk resistance (R_{bulk}) evinces that the ionic conductivity of the electrolyte improved at 90 °C.[43, 45, 47, 55] The resistance corresponding to the semicircle at the higher frequency region (R_1) also exhibited a slight decline during the elevated temperature operation—demonstrating of the amplified Na$^+$ migration across the cathode-electrolyte interface layer (CEI) layer.[59-61] However, the most significant decrease in resistance after temperature elevation was observed in the lower frequency region (R_2)—the interfacial resistance—indicative of improved interfacial phenomena at 90 °C.[57-58, 61-62] It is worth noting that the significant decrease of R_2 is a typical behavior for studying the temperature dependence of electrode materials. The activation energy on $1/R_2$ is very large compared to those for the other two resistances because the charge transfer process is more

sensitive to temperature increases.[45] The EIS data results here clearly show the interfacial resistance to be the dominant factor behind the limited capacity at 25 °C in IL electrolyte.

Although the NaFeF$_3$@C exhibits improved electrochemical activity at elevated temperatures, it is worth recalling that the crystallinity of this material was found to be diminished after the carbon-coating with AB. As such, it would be providential to investigate the effect of crystallinity on the electrochemical behavior of the orthorhombic NaFeF$_3$. To this end, charge-discharge measurements were performed on the RH-NaFeF$_3$@C (the sample subjected to a second heat treatment) electrode at 90 °C, as shown in Figure 3c. For a clear comparison with the NaFeF$_3$@C at 90 °C, the measurements were taken under the conditions previously prescribed. The charge-discharge curves of the first two cycles (Figure 3c-I) displayed two pairs of plateaus at 3.0 V and 3.4 V—akin to those observed in the NaFeF$_3$@C electrode (Figure 3a-I). However, the RH-NaFeF$_3$@C electrode delivered a vastly limited discharge capacity of 35 mAh g^{-1}, thereby confirming encumbered electrochemical activity. The poor charge-discharge behavior was further confirmed by the corresponding dQ/dV and GITT plots shown in Figure 3c-II and c-III. These results demonstrate that even though the same desodiation-sodiation processes in both electrode samples (NaFeF$_3$@C and RH-NaFeF$_3$@C) occurred *via* similar double two-phase reaction separated by an intermediate phase orthorhombic Na$_{0.5}$FeF$_3$, the RH-NaFeF$_3$@C electrode delivered a vastly limited activity. The poor performance observed here has been corroborated by

previous reports on FeF_3 electrodes in LIBs,[63] which have shown the samples with high crystallinity have large-sized particles that elongate cation (in this case Na^+) diffusion length.

The phase transformation and reaction mechanism(s) of the orthorhombic $NaFeF_3$ were further assessed by performing synchrotron XRD measurements (Figure 4a) in combination with Rietveld refinement on the charged/discharged electrodes (see Figure S5 for the refinement results and Table 1 for the refined parameters). The test electrodes at different SOCs were obtained from the initial charge-discharge cycle of a $Na/NaFeF_3@C$ half-cell at 90 °C, as shown by the potential-time profile in Figure 4b. As expected, the diffraction peak assigned to the PTFE binder used in electrode preparation appeared in all XRD patterns at $2\theta = 10.36°$.[16, 64] The Rietveld-refined parameters confirm the pristine $NaFeF_3@C$ electrode (Pattern 1) is indexed as an orthorhombic $NaFeF_3$ (Figure S5a and Table 1) with lattice parameters comparable to those of the $H-NaFeF_3$ and $NaFeF_3@C$ powder samples (Figure 2a,b and Table S1). After the electrode was half-charged to 3.2 V (Pattern 2), the diffraction peaks were observed to become broader than those in the pristine electrode. Rietveld refinement of the XRD diffraction peaks confirm the crystal structure to be an orthorhombic phase with a Na occupancy of 0.5 existing alongside an unreacted $NaFeF_3$ phase (Figure S5b and Table 1). The formation of the orthorhombic $Na_{0.5}FeF_3$ observed here is in good accord with previous theoretical works, validating the efficacy of the present results.[29-30] When the electrode was fully charged to 4.1 V (Pattern 3), all the diffraction peaks were seen to shift to higher angles, which suggests that a new phase was formed after complete desodiation. The new

phase was indexed as a cubic FeF_3 phase (rhenium trioxide structure) with the lattice parameter of $a = 3.8561(7)$ Å (Figure S5c and Table 1). It is worth noting that even though the transformation from nano-sized orthorhombic $NaFeF_3$ to cubic FeF_3 during desodiation has been previously reported,[31] this is the first time the existence of the orthorhombic $Na_{0.5}FeF_3$ as an intermediate phase in the desodaition process is experimentally detected at 90 °C.

Thereafter, XRD Pattern 4 was obtained from the electrode after half-discharge to 3.1 V. The diffraction peaks were noted to shift to angles lower than those in Pattern 3. The fitting results (Figure S5d and Table 1) revealed that a phase transformation from cubic FeF_3 back to orthorhombic $Na_{0.5}FeF_3$ had occurred during the discharge to 3.1 V. However, the orthorhombic $Na_{0.5}FeF_3$ formed during the sodiation of the cubic FeF_3 manifested smaller lattice parameters than those formed during the initial desodiation. Although several possibilities can be proposed for this phenomenon the most probably reason is the different Na composition in these phases owing to the existence of a solid-solution range. Upon further sodiation to 2.2 V (Pattern 5), the diffraction peaks shift back to their original positions, confirming that the orthorhombic $NaFeF_3$ structure was recovered. The lattice parameters of the recovered orthorhombic $NaFeF_3$ phase ($a = 5.6551(3)$ Å, $b = 7.8806(5)$ Å, and $c = 5.4849(3)$ Å) (Figure S5e and Table 1) were found to be comparable to those of the pristine $NaFeF_3$ electrode (Figure S5a and Table 1), suggesting that the phase transformation from orthorhombic $NaFeF_3$ to cubic FeF_3 during the desodiation-sodiation processes had good reversibility even though the orthorhombic $Na_{0.5}FeF_3$ compounds formed as

intermediate phase during the desodiation and sodiation, respectively, have different lattice parameters.

The long-term performance of the NaFeF$_3$@C electrode during elevated temperature (90 °C) operations was investigated by performing cycle tests on the Na/NaFeF$_3$@C half-cell at a current rate of 100 mA g^{-1} in the 2.2–4.0 V voltage range. As shown in Figure 5a, the NaFeF$_3$@C electrode exhibits long-term stability of up to 400 cycles, accompanied by a high average Coulombic efficiency of 99.9%. The NaFeF$_3$@C electrode achieved an initial discharge capacity of 152 mAh g^{-1}, which was noted to gradually decrease with the capacity retention of 82, 75, 64, 56, and 50% at the 50, 100, 200, 300, and 400th cycles, respectively. Although the capacity retention of this work is not excellent, the electrochemical performance measured at such a high current rate of 100 mA g^{-1} and a narrow voltage range of 2.2–4.0 V is still competitive (see Table S4).[65-68] The corresponding charge-discharge curves and dQ/dV plots (Figure 5b,c) show that the two plateaus (in the charge-discharge curves) were preserved throughout the cycling process, albeit with some degree of variation in their oxidation and reduction peak voltages. These results confirm that the multi-phase transition observed above is maintained throughout the cycles. However, the polarization gradually increased with continued cycling, presumably due to the significant changes in the lattice volume (volume ratio: orthorhombic NaFeF$_3$ / orthorhombic Na$_{0.5}$FeF$_3$ / cubic FeF$_3$ = 1.00 / 1.00 / 0.94) caused by the phase transformations between the orthorhombic NaFeF$_3$ and cubic FeF$_3$ phases during the charge and discharge processes.

19

The factors influencing the capacity decay during cycling were further investigated through EIS measurements conducted on the Na/NaFeF$_3$@C half-cell at the 0th, 1st, 10th, 50th, and 100th cycles at 90 °C (Figure S6). The impedance contributions of each element were quantified by fitting the Nyquist plots of the 1st and 100th cycles (Figure 5d) into the equivalent circuit in Figure 5e. As depicted by the fitting results in Figure 5f, the low values exhibited by all resistance components after the 1st charge-discharge cycle are seen to have increased after the 100th cycle: an attestation to the diminishing Na$^+$ kinetics with continued cycling. In particular, the low-frequency resistance component, R_2, exhibits a significantly larger increase compared to the R_{bulk} and R_1, suggesting that the cycle performance is mainly inhibited by the interfacial phenomenon.[57-58] This is also validated by the surface morphology of the NaFeF$_3$@C electrode after 400 cycles (see SEM images shown in Figure S7) As shown in Figure S7, NaFeF$_3$@C particles are covered by thick layers and the border of the particles is hard to be distinguished, which indicates the electrochemical decomposition of the IL electrolytes during cycling.[40, 52] Although the stable interfacial layer with appropriate thickness is conducive in the stable cycling,[52-53] large cracks on the surface of the NaFeF$_3$@C electrode after 400 cycles also leads to the unstable interfacial layer related to the capacity drop.[52, 56] Additionally, stable deposition-dissolution behavior of Na metal in the Na[FSA]-[C$_2$C$_1$im][FSA] IL electrolyte was confirmed over cycles in the previous studies,[39, 43, 69] which indicates that the effects of Na metal counter electrode is negligible in the EIS data.

Finally, the rate performance of the Na/NaFeF$_3$@C cell was investigated in the cutoff voltage range of 2.2−4.0 V at 90 °C (Figure S8). Here, the cell was charged at 20 mA g^{-1} and discharged at varied current rates of 20, 50, 100, 200, 500, 1000, and 20 mA g^{-1} for 5 cycles in each case. The results reveal that the NaFeF$_3$@C electrode yielded relatively higher discharge capacities at low current rates (150 mAh g^{-1} at 20 mA g^{-1}). In contrast, measurements at high current rates resulted in significantly lower discharge capacities (43.4 mAh g^{-1} at 1000 mA g^{-1})—a trend attributed to the large charge transfer resistance at the surface of NaFeF$_3$.

CONCLUSIONS

The present study reports an orthorhombic NaFeF$_3$ prepared through high-energy ball milling and heat treatment processes as a positive electrode for SIBs. Here, a thermally stable Na[FSA]-[C$_2$C$_1$im][FSA] IL electrolyte is employed to explore the electrochemical properties and reaction mechanism(s) of the orthorhombic NaFeF$_3$ at 90 °C. The NaFeF$_3$@C electrode attains a reversible capacity of 177 mAh g^{-1} (current rate: 10 mA g^{-1} and cutoff voltage range: 2.2−4.1 V) with curve-discharge curves characterized by two pairs of plateaus. A combination of GITT tests and synchrotron XRD analyses reveal that the two pairs of plateaus visualized in the charge-discharge curves correspond to multi-phase reaction(s) between orthorhombic NaFeF$_3$ and cubic FeF$_3$ through the intermediate orthorhombic Na$_{0.5}$FeF$_3$ phase. Additionally, the orthorhombic NaFeF$_3$ exhibits long-term cycle stability of up to 400 cycles conducted at a current density of 100 mA g^{-1}.

The first experimental validation of an intermediate orthorhombic $Na_{0.5}FeF_3$ phase represents a critical milestone in the advancements of Na-Fe-F systems. The high electrochemical activity and long-term cycling stability of the composite $NaFeF_3$ electrode during elevated temperature operations point to its possible application in large-scale devices. Even so, the reversibility of the multi-phase transformation during desodiation-sodiation processes still requires further improvement for enhanced electrode performance. However, it is worth noting that this work does not shed light on the Na^+ extraction/insertion path(s) from/into orthorhombic $NaFeF_3$/cubic FeF_3 but instead highlights the multi-phase transformation behavior influencing the $NaFeF_3$ performance. In this context, we establish that although the sodiation/desodiation processes recover the orthorhombic $NaFeF_3$, the phase evolution entails the formation of orthorhombic $Na_{0.5}FeF_3$ phases with different lattice parameters. We anticipate that further exploration into this phenomenon provides a deeper understanding of the Na-Fe-F system and aids in harnessing their enormous potential as next-generation energy devices.

Table 1. Crystallographic parameters of the phases at different SOCs (Patterns 1, 2, 3, 4, and 5 in Figure 4a) by Rietveld refinement.

Refinement results for the orthorhombic NaFeF$_3$ phase in Pattern 1[a] (S.G. *Pnma*) R_p = 1.67%, R_wp = 2.00%						
a = 5.6553(5) Å		b = 7.8858(7) Å		c = 5.4826(4) Å		V = 244.50(4) Å^3
Atom	Wyckoff	x	y	z	B_iso / Å^2	Occup.
Fe	4*a*	0	0	0	0.5	1
Na	4*c*	0.4448(3)	0.25	0.0117(9)	0.5	1
F1	4*c*	0.5675(8)	0.25	0.6018(8)	0.5	1
F2	8*d*	0.1919(6)	0.0575(4)	0.3011(6)	0.5	1
Refinement results for the orthorhombic Na$_{0.5}$FeF$_3$ phase in Pattern 2[b] (S.G. *Pnma*) R_p = 2.79%, R_wp = 3.87%						
a = 5.669(1) Å		b = 7.876(2) Å		c = 5.488(1) Å		V = 245.03(9) Å^3
Atom	Wyckoff	x	y	z	B_iso / Å^2	Occup.
Fe	4*a*	0	0	0	0.5	1
Na	4*c*	0.461(3)	0.25	0.028(4)	0.5	0.5
F1	4*c*	0.501(4)	0.25	0.568(2)	0.5	1
F2	8*d*	0.197(1)	0.101(1)	0.307(2)	0.5	1
Refinement results for the cubic FeF$_3$ phase in Pattern 3[c] (S.G. $Pm\bar{3}m$) R_p = 7.88%, R_wp = 10.29%						
a = 3.8561(7) Å				V = 57.34(3) Å^3		
Atom	Wyckoff	x	y	z	B_iso / Å^2	Occup.
Fe	1*a*	0	0	0	0.5	1
F	3*d*	0	0	0.5	0.5	1
Refinement results for the orthorhombic Na$_{0.5}$FeF$_3$ phase in Pattern 4[d] (S.G. *Pnma*) R_p = 2.78%, R_wp = 3.82%						
a = 5.5537(7) Å		b = 7.7910(9) Å		c = 5.4362(7) Å		V = 235.22(5) Å^3
Atom	Wyckoff	x	y	z	B_iso / Å^2	Occup.
Fe	4*a*	0	0	0	0.5	1
Na	4*c*	0.462(1)	0.25	-0.015(3)	0.5	0.5

Atom	Wyckoff	x	y	z	B_{iso} / Å²	Occup.
F1	4c	0.534(2)	0.25	0.572(1)	0.5	1
F2	8d	0.1981(8)	0.0512(7)	0.2889(9)	0.5	1

Refinement results for the orthorhombic NaFeF₃ phase in Pattern 5[e] (S.G. *Pnma*) R_p = 2.79%, R_{wp} = 3.51%						
a = 5.6551(3) Å		b = 7.8806(5) Å	c = 5.4849(3) Å		V = 244.44(3) Å³	
Atom	Wyckoff	x	y	z	B_{iso} / Å²	Occup.
Fe	4a	0	0	0	0.5	1
Na	4c	0.4464(3)	0.25	0.0158(6)	0.5	1
F1	4c	0.5495(6)	0.25	0.5998(6)	0.5	1
F2	8d	0.1972(4)	0.0582(3)	0.3027(4)	0.5	1

[a] Phase with no impurity. [b] Orthorhombic NaFeF₃ phase is considered to be impurity (28 wt%). [c] Phase with no impurity. [d] Phase with no impurity. [e] Phase with no impurity.
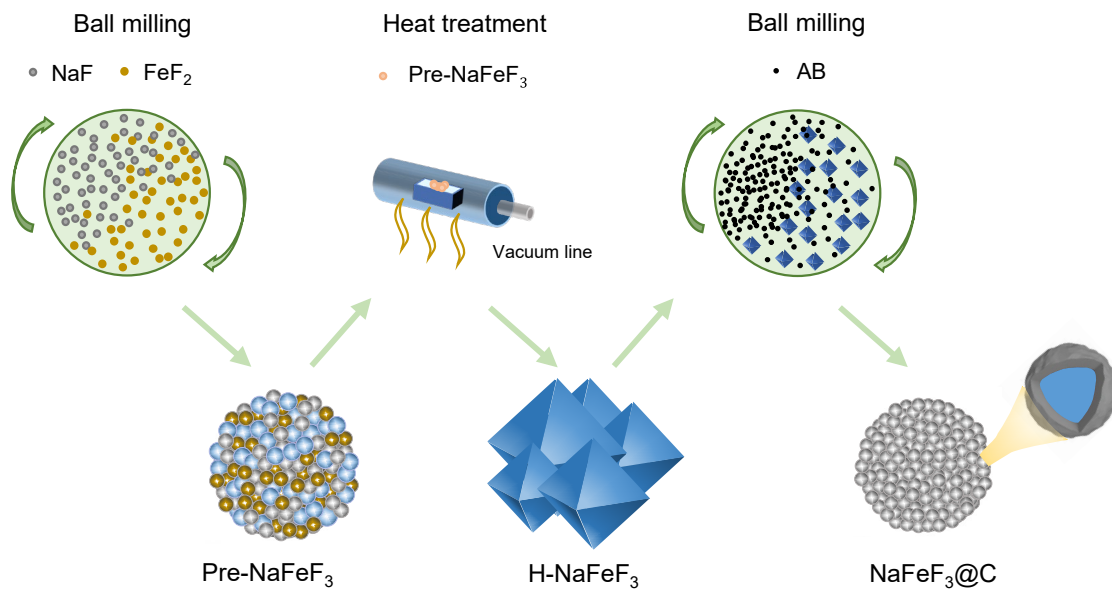
Figure 1. Schematic illustration of the orthorhombic $NaFeF_3$ preparation process. Step 1: Initial ball-milling of NaF and FeF_2 (Pre-$NaFeF_3$). Step 2: Heat Pre-$NaFeF_3$ at 600 °C for 24 h under vacuum (H-$NaFeF_3$). Step 3: Subsequent ball-milling of the H-$NaFeF_3$ and AB ($NaFeF_3$@C).
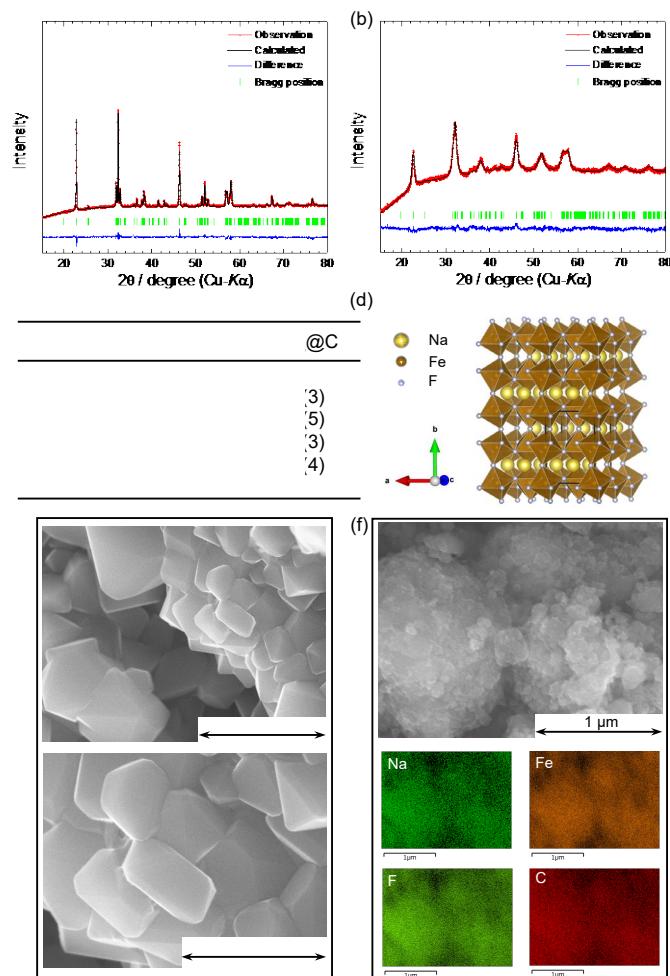
Figure 2. (a) XRD pattern and Rietveld refinement patterns of the H-NaFeF$_3$ sample (see Figure S1b as well). (b) XRD pattern and Rietveld refinement patterns of the NaFeF$_3$@C sample (see Figure S1c as well). (c) Rietveld-refined lattice parameters of the H-NaFeF$_3$ and NaFeF$_3$@C samples (see Table S1 for the crystallographic data). (d) Schematic of a refined orthorhombic NaFeF$_3$ crystal structure. (e) The corresponding SEM images of the H-NaFeF$_3$ particles. The bottom image is a magnification of the top one. (f) The corresponding SEM images of the NaFeF$_3$@C particles (top one) and EDX mappings (bottom ones) of Na, Fe, F, and C in the NaFeF$_3$@C sample.
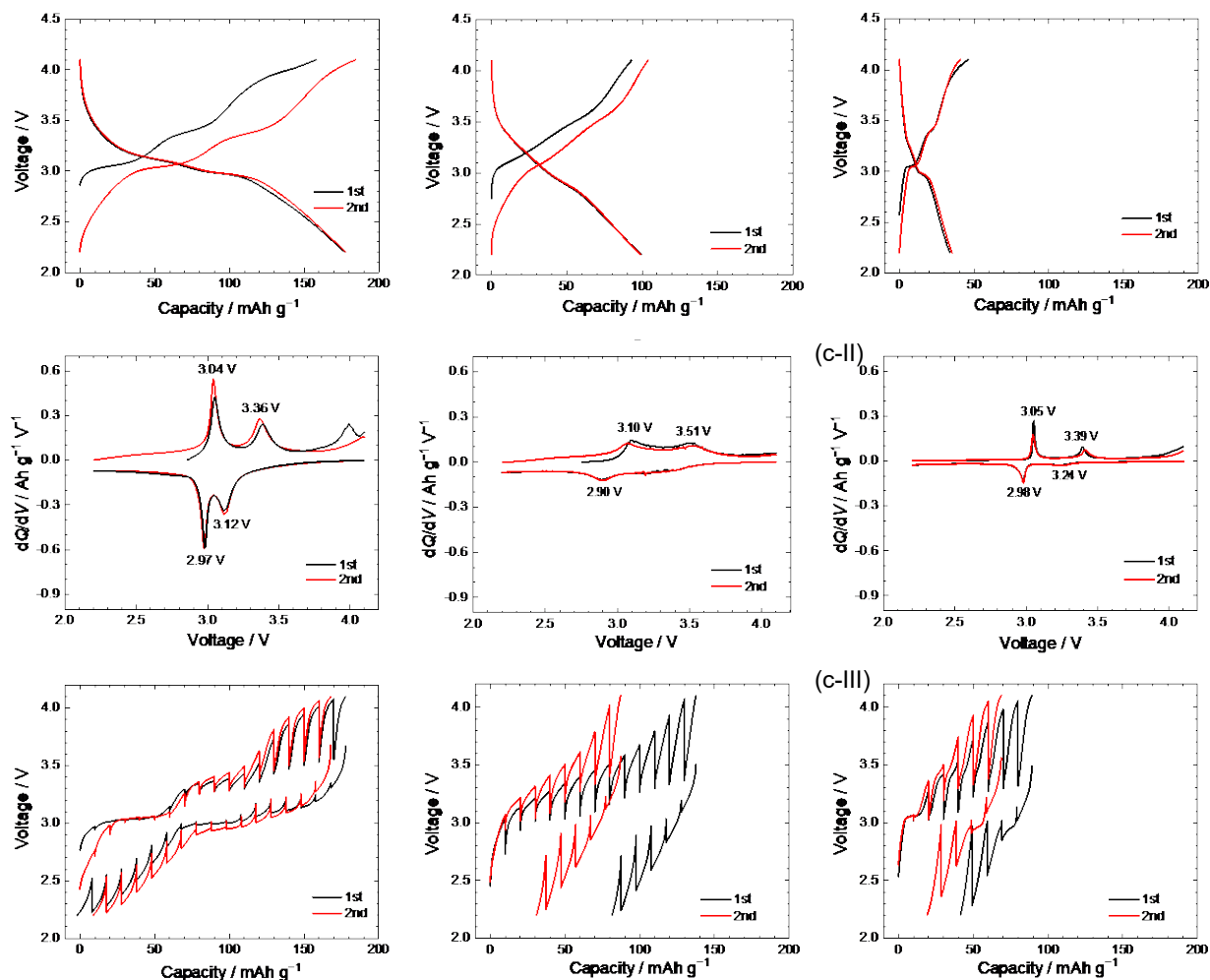
Figure 3. Electrochemical performance of (a) NaFeF$_3$@C at 90 °C, (b) NaFeF$_3$@C at 25 °C, and (c) RH-NaFeF$_3$@C at 90 °C using the Na[FSA]-[C$_2$C$_1$im][FSA] (20:80 in mol) IL electrolyte in the voltage range of 2.2−4.1 V. (I) Charge-discharge curves of the first two cycles at the current rate of 10 mA g^{-1}; (II) the corresponding dQ/dV plots of the charge-discharge curves in (I); and (III) the GITT curves obtained from a stepwise polarization of the half-cell at the current rate of 10 mA g^{-1} for 1 h proceeded by a 12 h monitoring of the open-circuit voltage.
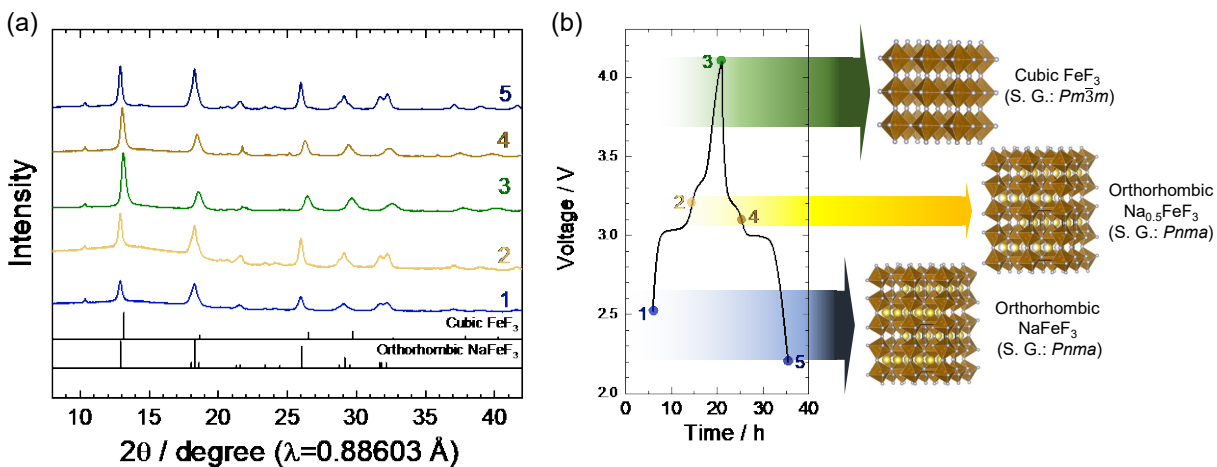
Figure 4. (a) Synchrotron XRD patterns ($\lambda = 0.88603$ Å) of the $NaFeF_3$@C electrode at different SOCs and (b) the corresponding initial charge and discharge voltage profiles at a current density of 10 mA g^{-1} in the Na[FSA]-[C$_2$C$_1$im][FSA] (20:80 in mol) IL electrolyte at 90 °C: (1) Pristine electrode, (2) electrode charged to 3.2 V, (3) electrode charged to 4.1 V, (4) electrode discharged to 3.1 V, and (5) electrode discharged to 2.2 V.
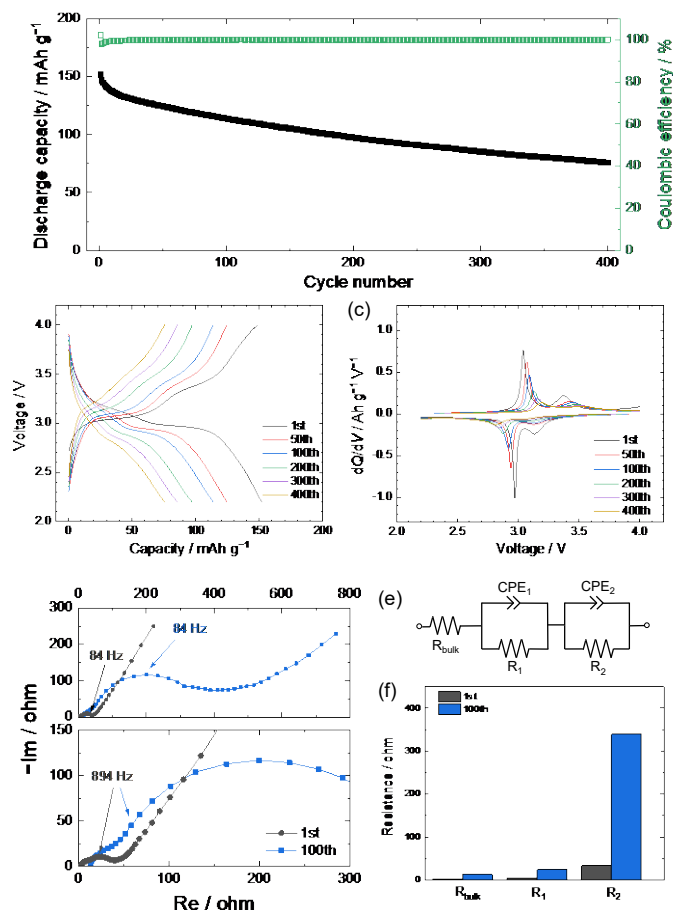
Figure 5. The electrochemical properties of the NaFeF$_3$@C electrode along with the Na[FSA]-[C$_2$C$_1$im][FSA] (20:80 in mol) IL electrolyte measured at 90 °C in the voltage range of 2.2−4.0 V. (a) The corresponding cycling performance over 400 cycles at a rate of 100 mA g^{-1}. (b) The charge-discharge curves were taken after the 1st, 50th,100th, 200th, 300th, and 400th. (c) The corresponding dQ/dV plots of the charge-discharge curves in (b). (d) Nyquist plots of the Na/NaFeF$_3$ half-cell taken after the 1st and 100th cycles. AC perturbation: 10 mV. Frequency range: 10 mHz–100 kHz. The bottom plot is a magnification of the top one. (e) The equivalent circuit used to fit the Nyquist plots in (d). (f) R_{bulk}, R_1, and R_2 were obtained by fitting the Nyquist plots in (d) (see Table S3 in Supporting Information for the fitting parameters).

29

ASSOCIATED CONTENT

Supporting Information. The Supporting Information is available free of charge on the ACS Publications website.

Crystallographic parameters of the orthorhombic $NaFeF_3$ phase; EIS data; comparison of electrochemical performance for $NaFeF_3$; XRD data; fit to synchrotron XRD data, and rate properties (PDF).

AUTHOR INFORMATION

Corresponding Author

*E-mail: k-matsumoto@energy.kyoto-u.ac.jp

ORCID

Yayun Zheng: 0000-0003-1036-7650

Jinkwang Hwang: 0000-0003-4800-3158

Kazuhiko Matsumoto: 0000-0002-0770-9210

Rika Hagiwara: 0000-0002-7234-3980

Notes

Any additional relevant notes should be placed here.

ACKNOWLEDGMENT

REFERENCES

(1) Li, M.; Lu, J.; Chen, Z.; Amine, K. 30 Years of Lithium-Ion Batteries. *Adv. Mater.* **2018,** *30*, 1800561.

(2) Li, Y.; Lu, Y.; Adelhelm, P.; Titirici, M. M.; Hu, Y. S. Intercalation chemistry of graphite: alkali metal ions and beyond. *Chem. Soc. Rev.* **2019,** *48*, 4655−4687.

(3) Wang, L. P.; Yu, L.; Wang, X.; Srinivasan, M.; Xu, Z. J. Recent developments in electrode materials for sodium-ion batteries. *J. Mater. Chem. A* **2015,** *3*, 9353−9378.

(4) Yu, L.; Wang, L. P.; Liao, H.; Wang, J.; Feng, Z.; Lev, O.; Loo, J. S. C.; Sougrati, M. T.; Xu, Z. J. Understanding Fundamentals and Reaction Mechanisms of Electrode Materials for Na-Ion Batteries. *Small* **2018,** *14*, 1703338.

(5) Sun, Y.; Guo, S.; Zhou, H. Exploration of Advanced Electrode Materials for Rechargeable Sodium‐Ion Batteries. *Adv. Energy Mater.* **2018,** *9*, 1800212.

(6) Gong, Z.; Yang, Y. Recent advances in the research of polyanion-type cathode materials for Li-ion batteries. *Energy Environ. Sci.* **2011,** *4*, 3223−3242.

(7) Conte, D. E.; Pinna, N. A review on the Application of Iron(III) Fluorides as Positive Electrodes for Secondary Cells. *Mater. Renew. Sustain. Energy* **2014,** *3*, 1−22.

(8) Omenya, F.; Zagarella, N. J.; Rana, J.; Zhang, H.; Siu, C.; Zhou, H.; Wen, B.; Chernova, N.

A.; Piper, L. F. J.; Zhou, G.; Whittingham, M. S. Intrinsic Challenges to the Electrochemical Reversibility of the High Energy Density Copper(II) Fluoride Cathode Material. *ACS Appl. Energy Mater.* **2019,** *2*, 5243−5253.

(9) Ni, D.; Fang, L.; Sun, W.; Shi, B.; Chen, X.; Li, H.; Wang, Z.; Sun, K. FeF$_2$@MHCS Cathodes with High Capacity and Fast Sodium Storage Based on Nanostructure Construction. *ACS Appl. Energy Mater.* **2020,** *3*, 10340−10348.

(10) Nishijima, M.; Gocheva, I. D.; Okada, S.; Doi, T.; Yamaki, J.-i.; Nishida, T. Cathode Properties of Metal Trifluorides in Li and Na Secondary Batteries. *J. Power Sources* **2009,** *190*, 558–562.

(11) Guntlin, C. P.; Zünd, T.; Kravchyk, K. V.; Wörle, M.; Bodnarchuk, M. I.; Kovalenko, M. V. Nanocrystalline FeF$_3$ and MF$_2$ (M = Fe, Co, and Mn) from Metal Trifluoroacetates and their Li(Na)-Ion Storage Properties. *J. Mater. Chem. A* **2017,** *5*, 7383−7393.

(12) Murugesan, V.; Cho, J. S.; Govind, N.; Andersen, A.; Olszta, M. J.; Han, K. S.; Li, G.; Lee, H.; Reed, D. M.; Sprenkle, V. L.; Cho, S.; Nune, S. K.; Choi, D. Lithium Insertion Mechanism in Iron Fluoride Nanoparticles Prepared by Catalytic Decomposition of Fluoropolymer. *ACS Appl. Energy Mater.* **2019,** *2*, 1832−1843.

(13) Doe, R. E.; Persson, K. A.; Meng, Y. S.; Ceder, G. First-Principles Investigation of the Li-Fe-F Phase Diagram and Equilibrium and Nonequilibrium Conversion Reactions of Iron Fluorides

with Lithium. *Chem. Mater.* **2008,** *20*, 5274–5283.

(14) Yamakawa, N.; Jiang, M.; Key, B.; Grey, C. P. Identifying the Local Structures Formed during Lithiation of the Conversion Material, Iron Fluoride, in a Li Ion Battery: A Solid-State NMR, X-ray Diffraction, and Pair Distribution Function Analysis Study. *J. Am. Chem. Soc.* **2009,** *131*, 10525−10536.

(15) Li, L.; Jacobs, R.; Gao, P.; Gan, L.; Wang, F.; Morgan, D.; Jin, S. Origins of Large Voltage Hysteresis in High-Energy-Density Metal Fluoride Lithium-Ion Battery Conversion Electrodes. *J. Am. Chem. Soc.* **2016,** *138*, 2838–2848.

(16) Zheng, Y.; Tawa, S.; Hwang, J.; Orikasa, Y.; Matsumoto, K.; Hagiwara, R. Phase evolution of trirutile $Li_{0.5}FeF_3$ for lithium-ion batteries. *Chem. Mater.* **2021,** *33*, 868−880.

(17) Tawa, S.; Sato, Y.; Orikasa, Y.; Matsumoto, K.; Hagiwara, R. Lithium Fluoride/Iron Difluoride Composite Prepared by a Fluorolytic Sol–Gel Method: Its Electrochemical Behavior and Charge–Discharge Mechanism as a Cathode Material for Lithium Secondary Batteries. *J. Power Sources* **2019,** *412*, 180–188.

(18) Xiao, A. W.; Lee, H. J.; Capone, I.; Robertson, A.; Wi, T. U.; Fawdon, J.; Wheeler, S.; Lee, H. W.; Grobert, N.; Pasta, M. Understanding the Conversion Mechanism and Performance of Monodisperse FeF_2 Nanocrystal Cathodes. *Nature Mater.* **2020,** *19*, 644–654.

(19) Zheng, Y.; Hwang, J.; Matsumoto, K.; Hagiwara, R. Charge-discharge properties and reaction mechanism of cation-disordered rutile-type $Li_{1.2}MnF_{e1.2}F_{6.8}$. *Electrochim. Acta* **2022,** *405*, 139627.

(20) Li, C.; Yin, C.; Gu, L.; Dinnebier, R. E.; Mu, X.; van Aken, P. A.; Maier, J. An $FeF_3 \bullet 0.5H_2O$ Polytype: A Microporous Framework Compound with Intersecting Tunnels for Li and Na Batteries. *J. Am. Chem. Soc.* **2013,** *135*, 11425−11428.

(21) Li, C.; Yin, C.; Mu, X.; Maier, J. Top-Down Synthesis of Open Framework Fluoride for Lithium and Sodium Batteries. *Chem. Mater.* **2013,** *25*, 962–969.

(22) Liu, L.; Guo, H.; Zhou, M.; Wei, Q.; Yang, Z.; Shu, H.; Yang, X.; Tan, J.; Yan, Z.; Wang, X. A comparison among $FeF_3 \cdot 3H_2O$, $FeF_3 \cdot 0.33H_2O$ and FeF_3 cathode materials for lithium ion batteries: Structural, electrochemical, and mechanism studies. *J. Power Sources* **2013,** *238*, 501−515.

(23) Shen, Y.; Wang, X.; Hu, H.; Jiang, M.; Yang, X.; Shu, H. A Graphene Loading Heterogeneous Hydrated Forms Iron based Fluoride Nanocomposite as Novel and High-Capacity Cathode Material for Lithium/Sodium Ion Batteries. *J. Power Sources* **2015,** *283*, 204−210.

(24) Wei, S.; Wang, X.; Jiang, M.; Zhang, R.; Shen, Y.; Hu, H. The $FeF_3 \cdot 0.33H_2O$/C Nanocomposite with Open Mesoporous Structure as High-Capacity Cathode Material for Lithium/Sodium Ion Batteries. *J. Alloys Compd.* **2016,** *689*, 945−951.

(25) Zhang, R.; Wang, X.; Wang, X.; Liu, M.; Wei, S.; Wang, Y.; Hu, H. Iron Fluoride Packaged into 3D Order Mesoporous Carbons as High-Performance Sodium-Ion Battery Cathode Material. *J. Electrochem. Soc.* **2018,** *165*, A89−A96.

(26) Liu, M.; Liu, L.; Hu, H.; Yang, L.; Yang, Z.; Wang, Y.; Wang, X. Flowerlike Mesoporous $FeF_3 \cdot 0.33H_2O$ with 3D Hierarchical Nanostructure: Size-Controlled Green-Synthesis and Application as Cathodes for Na-Ion Batteries. *ACS Appl. Energy Mater.* **2018,** *1*, 7153−7163.

(27) Liu, M.; Liu, L.; Li, M.; Chen, B.; Lei, H.; Hu, H.; Wang, X. Preparation and Li/Na Ion Storage Performance of Raspberry-like Hierarchical $FeF_3 \cdot 0.33H_2O$ Micro-Sized Spheres with Controllable Morphology. *J. Alloys Compd.* **2020,** *829*, 1−10.

(28) Sun, Z.; Fu, W.; Liu, M. Z.; Lu, P.; Zhao, E.; Magasinski, A.; Liu, M.; Luo, S.; McDaniel, J.; Yushin, G. A nanoconfined iron(iii) fluoride cathode in a NaDFOB electrolyte: towards high-performance sodium-ion batteries. *J. Mater. Chem. A* **2020,** *8*, 4091−4098.

(29) Yu, S.; Zhang, P.; Wu, S. Q.; Li, A. Y.; Zhu, Z. Z.; Yang, Y. Understanding the Structural and Electronic Properties of the Cathode Material $NaFeF_3$ in A Na-Ion Battery. *J. Solid State Electrochem.* **2014,** *18*, 2071–2075.

(30) Kitajou, A.; Ishado, Y.; Yamashita, T.; Momida, H.; Oguchi, T.; Okada, S. Cathode Properties of Perovskite-type $NaMF_3$ (M = Fe, Mn, and Co) Prepared by Mechanical Ball Milling for Sodium-ion Battery. *Electrochim. Acta* **2017,** *245*, 424–429.

(31) Martin, A.; Doublet, M.-L.; Kemnitz, E.; Pinna, N. Reversible Sodium and Lithium Insertion in Iron Fluoride Perovskites. *Adv. Funct. Mater.* **2018,** *28*, 1802057.

(32) Ma, D.-l.; Wang, H.-g.; Li, Y.; Xu, D.; Yuan, S.; Huang, X.-l.; Zhang, X.-b.; Zhang, Y. In situ Generated FeF_3 in Homogeneous Iron Matrix toward High-Performance Cathode Material for Sodium-Ion Batteries. *Nano Energy* **2014,** *10*, 295–304.

(33) Zheng, Y.; Hwang, J.; Matsumoto, K.; Hagiwara, R. Electrochemical and Structural Behavior of Trirutile-Derived FeF_3 During Sodiation and Desodiation. *ACS Appl. Energy Mater.* **2022**, *5*, 3137−3145.

(34) Hwang, J.; Matsumoto, K.; Orikasa, Y.; Katayama, M.; Inada, Y.; Nohira, T.; Hagiwara, R. Crystalline maricite $NaFePO_4$ as a positive electrode material for sodium secondary batteries operating at intermediate temperature. *J. Power Sources* **2018,** *377*, 80–86.

(35) Zheng, Y.; Tawa, S.; Hwang, J.; Orikasa, Y.; Matsumoto, K.; Hagiwara, R. Phase Evolution of Trirutile $Li_{0.5}FeF_3$ for Lithium-Ion Batteries. *Chem. Mater.* **2021,** *33*, 868−880.

(36) Chancelier, L.; Diallo, A. O.; Santini, C. C.; Marlair, G.; Gutel, T.; Mailley, S.; Len, C. Targeting adequate thermal stability and fire safety in selecting ionic liquid-based electrolytes for energy storage. *Phys. Chem. Chem. Phys.* **2014,** *16*, 1967−76.

(37) Rodrigues, M.-T. F.; Babu, G.; Gullapalli, H.; Kalaga, K.; Sayed, F. N.; Kato, K.; Joyner, J.; Ajayan, P. M. A materials perspective on Li-ion batteries at extreme temperatures. *Nat. Energy*

2017, *2*, 1−14.

(38) Hwang, J.; Matsumoto, K.; Hagiwara, R. $Na_3V_2(PO_4)_3$/C Positive Electrodes with High Energy and Power Densities for Sodium Secondary Batteries with Ionic Liquid Electrolytes that Operate Across wide Temperature Ranges. *Adv. Sustainable Syst.* **2018,** *2*, 1700171.

(39) Matsumoto, K.; Hwang, J.; Kaushik, S.; Chen, C.-Y.; Hagiwara, R. Advances in Sodium Secondary Batteries utilizing Ionic Liquid Electrolytes. *Energy Environ. Sci.* **2019,** *12*, 3247–3287.

(40) Zheng, Y.; Wang, D.; Kaushik, S.; Zhang, S.; Wada, T.; Hwang, J.; Matsumoto, K.; Hagiwara, R. Ionic Liquid Electrolytes for Next-generation Electrochemical Energy Devices. *EnergyChem* **2022,** *4*, 100075.

(41) Torimoto, T.; Tsuda, T.; Okazaki, K.; Kuwabata, S. New frontiers in materials science opened by ionic liquids. *Adv. Mater.* **2010,** *22*, 1196−221.

(42) MacFarlane, D. R.; Tachikawa, N.; Forsyth, M.; Pringle, J. M.; Howlett, P. C.; Elliott, G. D.; Davis, J. H.; Watanabe, M.; Simon, P.; Angell, C. A. Energy applications of ionic liquids. *Energy Environ. Sci.* **2014,** *7*, 232−250.

(43) Matsumoto, K.; Hosokawa, T.; Nohira, T.; Hagiwara, R.; Fukunaga, A.; Numata, K.; Itani, E.; Sakai, S.; Nitta, K.; Inazawa, S. The Na[FSA]–[C_2C_1im][FSA] (C_2C_1im$^+$:1-ethyl-3-methylimidazolium and FSA$^−$:bis(fluorosulfonyl)amide) Ionic Liquid Electrolytes for Sodium Secondary Batteries. *J. Power Sources* **2014,** *265*, 36–39.

(44) Matsumoto, K.; Okamoto, Y.; Nohira, T.; Hagiwara, R. Thermal and Transport Properties of Na[N(SO$_2$F)$_2$]–[N-Methyl-N-propylpyrrolidinium][N(SO$_2$F)$_2$] Ionic Liquids for Na Secondary Batteries. *J. Phys. Chem. C* **2015,** *119,* 7648–7655.

(45) Hwang, J.; Matsumoto, K.; Hagiwara, R. Symmetric Cell Electrochemical Impedance Spectroscopy of Na$_2$FeP$_2$O$_7$ Positive Electrode Material in Ionic Liquid Electrolytes. *J. Phys. Chem. C* **2018,** *122,* 26857−26864.

(46) Hagiwara, R.; Matsumoto, K.; Hwang, J.; Nohira, T. Sodium Ion Batteries using Ionic Liquids as Electrolytes. *Chem. Rec.* **2018,** *19,* 758–770.

(47) Hwang, J.; Matsumoto, K.; Hagiwara, R. Electrolytes toward High-Voltage Na$_3$V$_2$(PO$_4$)$_2$F$_3$ Positive Electrode Durable against Temperature Variation. *Adv. Energy Mater.* **2020,** *10,* 2001880.

(48) Toby, B. H. EXPGUI, A Graphical User Interface for GSAS. *J. Appl. Cryst.* **2001,** *34,* 210−213.

(49) Momma, K.; Izumi, F. VESTA 3 for three-dimensional visualization of crystal, volumetric and morphology data. *J. Appl. Cryst.* **2011,** *44,* 1272−1276.

(50) Martin, A.; Santiago, E. S.; Kemnitz, E.; Pinna, N. Reversible Insertion in AFeF$_3$ (A = K$^+$, NH$_4^+$) Cubic Iron Fluoride Perovskites. *ACS Appl. Mater. Interfaces* **2019,** *11,* 33132−33139.

(51) Bernal, F. L. M.; Gonano, B.; Lundvall, F.; Wragg, D. S.; Fjellvåg, H. Canted

antiferromagnetism in high purity $NaFeF_3$ prepared by a novel wetchemical synthesis method. *Phys. Rev. Materials* **2020,** *4*, 1−9.

(52) Jin, Y.; Xu, Y.; Le, P. M. L.; Vo, T. D.; Zhou, Q.; Qi, X.; Engelhard, M. H.; Matthews, B. E.; Jia, H.; Nie, Z.; Niu, C.; Wang, C.; Hu, Y.; Pan, H.; Zhang, J.-G. Highly Reversible Sodium Ion Batteries Enabled by Stable Electrolyte-Electrode Interphases. *ACS Energy Lett.* **2020,** *5*, 3212−3220.

(53) Moeez, I.; Susanto, D.; Chang, W.; Lim, H.-D.; Chung, K. Y. Artificial cathode electrolyte interphase by functional additives toward long-life sodium-ion batteries. *Chem. Eng. J.* **2021,** *425*, 130547.

(54) Shi, Y.-L.; Shen, M.-F.; Xu, S.-D.; Qiu, X.-Y.; Jiang, L.; Qiang, Y.-H.; Zhuang, Q.-C.; Sun, S.-G. Electrochemical Impedance Spectroscopic Study of the Electronic and Ionic Transport Properties of NiF_2/C Composites. *Int. J. Electrochem. Sci.* **2011,** *6*, 3399−3415.

(55) Wohde, F.; Balabajew, M.; Roling, B. Li^+ Transference Numbers in Liquid Electrolytes Obtained by Very-Low-Frequency Impedance Spectroscopy at Variable Electrode Distances. *J. Electrochem. Soc.* **2016,** *163*, A714−A721.

(56) Zhang, W.; Richter, F. H.; Culver, S. P.; Leichtweiss, T.; Lozano, J. G.; Dietrich, C.; Bruce, P. G.; Zeier, W. G.; Janek, J. Degradation Mechanisms at the $Li_{10}GeP_2S_{12}$/$LiCoO_2$ Cathode Interface in an All-Solid-State Lithium-Ion Battery. *ACS Appl. Mater. Interfaces* **2018,** *10*,

22226−22236.

(57) Bredar, A. R. C.; Chown, A. L.; Burton, A. R.; Farnum, B. H. Electrochemical Impedance Spectroscopy of Metal Oxide Electrodes for Energy Applications. *ACS Appl. Energy Mater.* **2020,** *3*, 66−98.

(58) Charles-Blin, Y.; Nemoto, K.; Zettsu, N.; Teshima, K. Effects of a solid electrolyte coating on the discharge kinetics of a $LiCoO_2$ electrode: mechanism and potential applications. *J. Mater. Chem. A* **2020,** *8*, 20979−20986.

(59) Chen, C. H.; Liu, J.; Amine, K. Symmetric cell approach and impedance spectroscopy of high power lithium-ion batteries. *J. Power Sources* **2001,** *96*, 321−328.

(60) Andre, D.; Meiler, M.; Steiner, K.; Wimmer, C.; Soczka-Guth, T.; Sauer, D. U. Characterization of high-power lithium-ion batteries by electrochemical impedance spectroscopy. I. Experimental investigation. *J. Power Sources* **2011,** *196*, 5334−5341.

(61) Choi, W.; Shin, H.-C.; Kim, J. M.; Choi, J.-Y.; Yoon, W.-S. Modeling and Applications of Electrochemical Impedance Spectroscopy (EIS) for Lithium-ion Batteries. *J. Electrochem. Sci. Technol.* **2020,** *11*, 1−13.

(62) Qu, D.; Wang, G.; Kafle, J.; Harris, J.; Crain, L.; Jin, Z.; Zheng, D. Electrochemical Impedance and its Applications in Energy-Storage Systems. *Small Methods* **2018,** *2*, 1−27.

(63) Tawa, S.; Yamamoto, T.; Matsumoto, K.; Hagiwara, R. Iron(III) fluoride synthesized by a fluorolysis method and its electrochemical properties as a positive electrode material for lithium secondary batteries. *J. Fluorine Chem.* **2016,** *184*, 75−81.

(64) Kim, M.; Lee, S.; Kang, B. Fast-Rate Capable Electrode Material with Higher Energy Density than LiFePO$_4$: 4.2 V LiVPO$_4$F Synthesized by Scalable Single-Step Solid-State Reaction. *Adv. Sci.* **2016,** *3*, 1500366.

(65) Kitajou, A.; Komatsu, H.; Chihara, K.; Gocheva, I. D.; Okada, S.; Yamaki, J.-i. Novel synthesis and electrochemical properties of perovskite-type NaFeF$_3$ for a sodium-ion battery. *J. Power Sources* **2012,** *198*, 389−392.

(66) Dimov, N.; Nishimura, A.; Chihara, K.; Kitajou, A.; Gocheva, I. D.; Okada, S. Transition Metal NaMF$_3$ Compounds as Model Systems for Studying the Feasibility of Ternary Li-M-F and Na-M-F Single Phases as Cathodes for Lithium–Ion and Sodium–Ion Batteries. *Electrochim. Acta* **2013,** *110*, 214−220.

(67) Kravchyk, K. V.; Zünd, T.; Wörle, M.; Kovalenko, M. V.; Bodnarchuk, M. I. NaFeF$_3$ Nanoplates as Low-Cost Sodium and Lithium Cathode Materials for Stationary Energy Storage. *Chem. Mater.* **2018,** *30*, 1825–1829.

(68) Liu, W.; Wang, W.; Qin, M.; Shen, B. Successive synthesis and electrochemical properties of Na$_3$FeF$_6$ and NaFeF$_3$/C cathode materials for lithium-ion and sodium-ion batteries. *Ceram. Int.*

2020, *46*, 11436−11440.

(69) Hosokawa, T.; Matsumoto, K.; Nohira, T.; Hagiwara, R.; Fukunaga, A.; Sakai, S.; Nitta, K. Stability of Ionic Liquids against Sodium Metal: A Comparative Study of 1-Ethyl-3-methylimidazolium Ionic Liquids with Bis(fluorosulfonyl)amide and Bis(trifluoromethylsulfonyl)amide. *J. Phys. Chem. C* **2016,** *120*, 9628−9636.

TOC graphic